Chapter 2

FINITE ELEMENT MODELING OF A RAT SPINAL CORD

In this chapter, I will discuss applying finite element modeling to the problem of modeling epidural stimulation in the lumbar portion of a rat spinal cord. Briefly, magnetic resonance imaging (MRI) was used to obtain images of a rat spinal cord (Section 2.1). Tissue images were segmented and a transverse slice through the L1 vertebra was used to extrude a 3D spinal model which was coupled with electrodes in SolidWorks (Section 2.1.1). Stimulation waveforms were analyzed for their dominant frequency components (Section 2.1.3). Material properties (conductivity and permittivity) were determined (Section 2.1.4) using the main frequency component of each stimulation waveform. Section 2.2 describes a volume conductor simulation using the COMSOL environment. This section also uses spatial symmetries and translations in the bipolar electrode combinations in order to reduce the number of simulated combinations to 18. Section 2.2.2 briefly discusses computational details of running the simulations. Section 2.A presents a summary of conductivity and permittivity data from the literature.

2.1 Building the 3D volume conductor model

To provide a realistic simulation model, the geometry of the lumbosacral spinal cord and its surrounding tissue was derived from MRI scans of a rat. An adult female Sprague Dawley rat (a control animal from another lab already scheduled to be euthanized) was fixed with 4% paraformaldehyde. The legs, tail, and everything rostral from the T12 vertebra was removed. The remaining spinal cord and muscle tissue was soaked for about 6 days in 3% $K_2(Cr_2O_7)$ and 10-mM Gd-HP-DO3A following (Zhang et al., 2010). After soaking, it was placed in a solution containing

perfluoropolyether (Galden®) to maintain the staining. The sample was imaged in an 11.7 tesla MRI machine at the Caltech Center for Biological Imaging at a voxel resolution of 78 µm. Vertebrae T13, L1, L2, L3, and L4 were manually identified in the resulting scans and segmented by hand (labeling bone and the inside of the bone, see Figs. 2.1 and 2.2). Segmentation was done using the Matlab NIFTI[a] toolbox and the bioelectromagnetism Toolbox[b] to select regions of interest, and ITK-SNAP[c] (Yushkevich et al., 2006) to segment the regions. Custom Matlab code was then used to merge the segmentation labels back into a single 3D image.

2.1.1 2d extrusion model with embedded electrode array model

Rather than model the full 3D structure of the rat spine shown in Figs. 2.1 and 2.2, it was decided to model a 3 by 7 electrode array embedded in a 3D extrusion of a spinal cord MRI slice taken from the middle of the L1 vertebra. This simplified model reduced the complexity of the simulations while maintaining the applicability to the L1 region. The area of the spinal cord under the L1 vertebra is known (Parag Gad, Choe, et al., 2013) to contain the motor pools for the soleus, tibialis anterior, and medial gastrocnemius muscles.

The manual segmentation of a transverse spinal cord slice from the middle of the L1 vertebra can be seen in Fig. 2.3. Gray matter and white matter were clearly visible in in the MRI data. Some spinal roots and nerve fibers were visible in the Cerebrospinal fluid (CSF). Preliminary COMSOL simulations including the fibers as cylinders of white matter in the CSF showed minimal effect on the voltage distribution inside the spinal cord (white/gray matter), so these fibers were left out from the final simulation model. Epidural fat was not visible in the MRI images. During the surgical implantation of epidural electrodes in rat models, the epidural fat

[a] http://www.mathworks.com/matlabcentral/fileexchange/8797-tools-for-nifti-and-analyze-image

[b] http://eeg.sourceforge.net/bioelectromagnetism.html

[c] www.itksnap.org

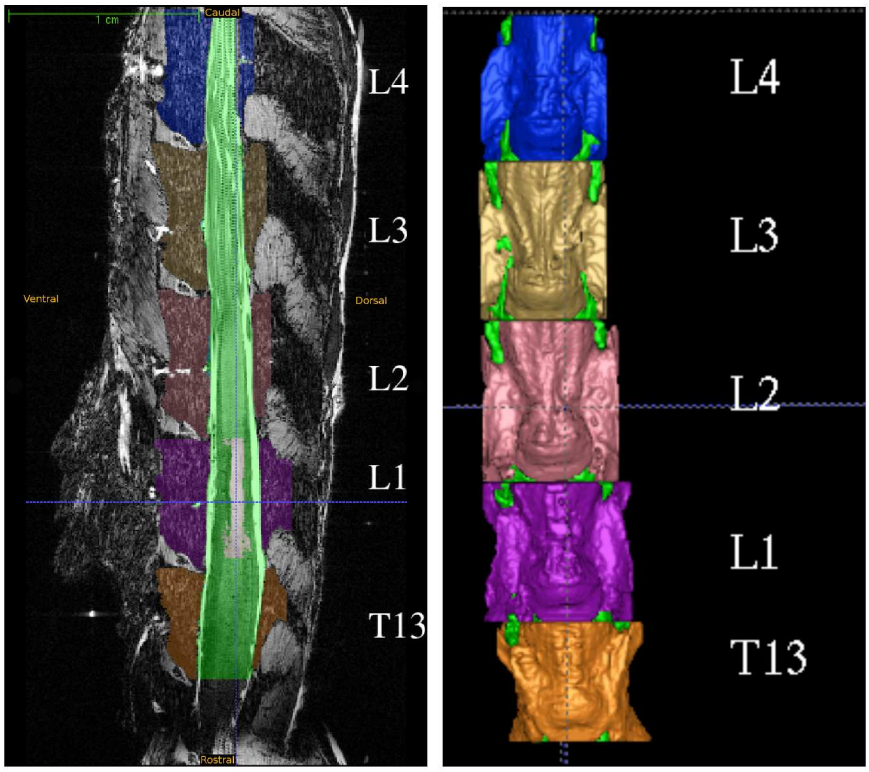

(a) Sagittal slice (b) 3D mesh of segmented vertebra

Figure 2.1: MRI data of the spinal cord of an adult female Sprague Dawley rat showing vertebra T13-L4. The vertebra are labeled with colors: L4, L3, L2, L1, and T13. The CSF, white matter, gray matter, and nerve fibers are labeled green except for the L1 gray matter which is uncolored. Subfigures: (a) shows a sagittal slice (down the middle of the spinal cord) with the dorsal direction to the right, the ventral direction to the left, the rostral direction to the top, and the caudal direction to the bottom of the page. (b) shows a 3D mesh representation of the segmented data.

is usually removed from the region that the electrode array will sit over. In other regions, the epidural fat would be next to vertebral bone, which has a conductivity more similar to epidural fat than to CSF. Therefore the epidural fat was left out of the simulation. Bone and muscle are also visible in the MRI slice. The gray matter, CSF, and bone can be modeled as isotropic. Muscles and white matter on the other hand have mostly parallel internal fibers which allow for increased conduction along the fibers and reduced conduction perpendicular to the fibers. In the spinal white matter, the myelinated axons run primarily along the rostral-caudal direction.

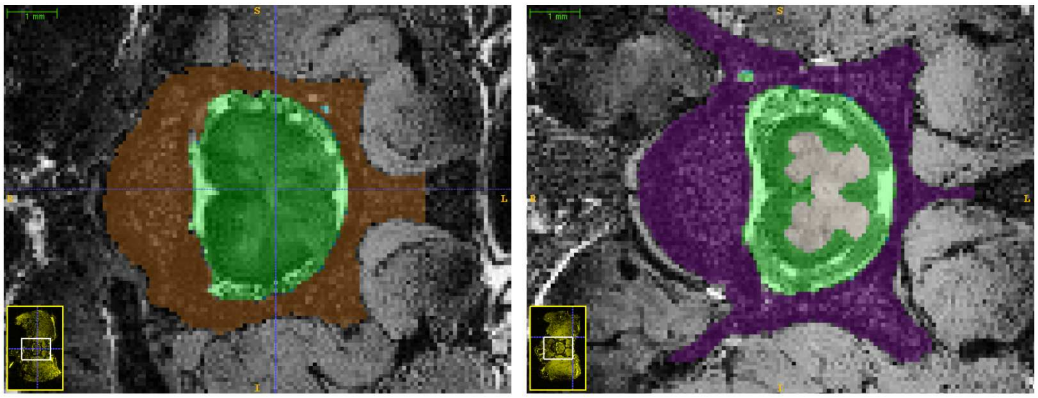

(a) T13 (b) L1

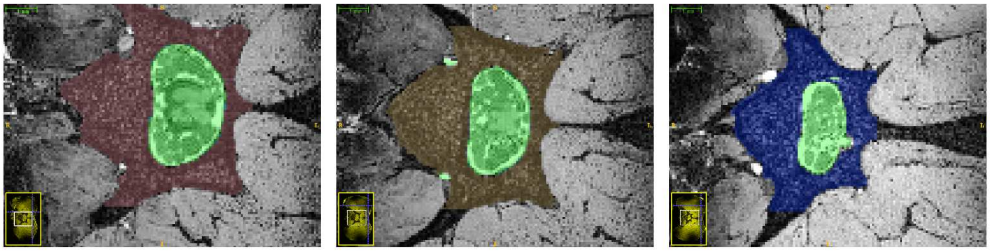

(c) L2 (d) L3 (e) L4

Figure 2.2: Transverse slices of the MRI data of the spinal cord of an adult female Sprague Dawley. Each subfigure shows a slice in the approximate middle of each vertebra: (a) T13 vertebra, (b) L1 vertebra, (c) L2 vertebra, (d) L3 vertebra, and (e) L4 vertebra. The CSF, white matter, gray matter, and nerve fibers are labeled green except for the L1 gray matter which is uncolored. The dorsal direction is to the right of the page.

For muscle fibers, the attachment of muscle to the vertebra is more complex, but appeared to mostly contain fibers parallel to the rostral-caudal axis in the region near the spinal cord.

This model will be used throughout the rest of the thesis and uses an x, y, z coordinate system defined such that:

- $+\hat{x}$ points to the animal's right side
- $-\hat{x}$ points to the animal's left side
- $+\hat{y}$ points in the dorsal direction
- $-\hat{y}$ points in the ventral direction

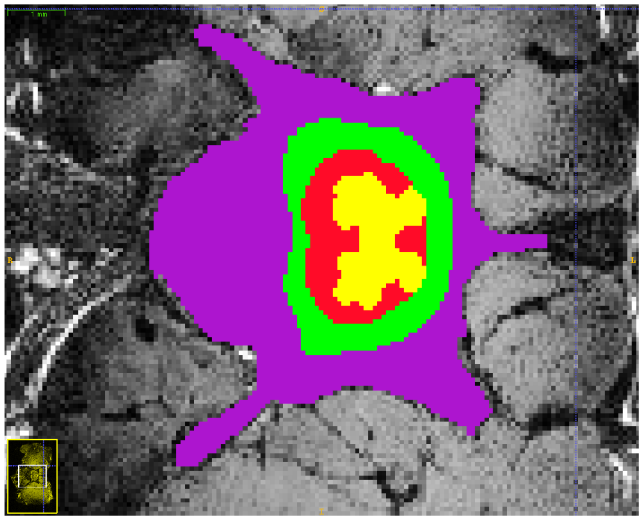

Figure 2.3: Transverse MRI slice of rat spinal cord from the middle of L1 vertebra. The dorsal direction is to the right of the page. Materials are labeled with colors: gray matter (yellow), white matter (red), cerebrospinal fluid (CSF)/roots/fibers (green), and bone (purple).

- $+\hat{z}$ points in the caudal direction
- $-\hat{z}$ points in the rostral direction

2.1.2 Electrical and physical model of epidural stimulating arrays

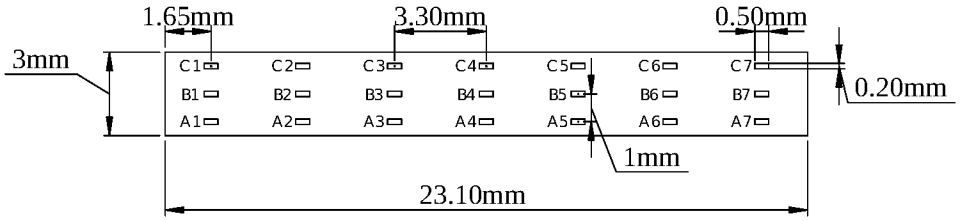

Figure 2.4: Dimensions of flat electrode array. The small (0.50 mm by 0.20 mm) rectangles are the platinum electrodes. See Table 2.1 for electrode labels and array orientation. Figures 4.1 and 4.2 show the labeled electrode array in the simulated spinal cord.

The parameters of the model's multi-electrode epidural stimulating array were based on those found in (Parag Gad, Choe, et al., 2013). Specifically, rectangular platinum electrodes (500 µm by 200 µm) spaced 1 mm laterally (when flat, center to center) and 3.3 mm rostral-caudally were modeled (when flat, center to center). Figure 2.4 shows the dimensions of the flat array. See Table 2.1 for electrode labels

Column Letters: A B C

row #					
1	A1	B1	C1	$\hat{z}\downarrow$	cranial↑
2	A2	B2	C2		
3	A3	B3	C3		
4	A4	B4	C4		
5	A5	B5	C5		
6	A6	B6	C6		
7	A7	B7	C7		caudal↓

$\hat{x}\rightarrow$
←left side right side→
$\odot\ \hat{y}$, dorsal
$\otimes$ ventral

Table 2.1: This table shows the names of the electrodes and the orientation of the array in the spinal cord as if you are looking down at the back of the rat with its head pointed towards the top of the page. (Note that $\odot$ means that the dorsal direction is pointing out of the page and the $\otimes$ symbol indicates that the ventral direction is into the page.) Figures 4.1 and 4.2 show the labeled electrode array in the simulated spinal cord.

and array orientation. Figures 4.1 and 4.2 show the labeled electrode array in the simulated spinal cord. (See also Section 2.2.1 for discussion of electrode array combinations and combination naming.) Based on Figure 6 of (Parag Gad, Choe, et al., 2013), the center 5 rows of electrodes would cover the spinal region of L4, L5, L6, and S1. The parylene C backing of the electrode array is normally 20 µm thick (Parag Gad, Choe, et al., 2013). In order to simulate efficiently (and reduce the number of necessary mesh points), the parylene C thickness was chosen to be 40 µm and the electrode (platinum) thickness chosen to be 10 µm (normally 0.2 µm). A slice through the extruded model showing the thicker array can be seen in Figs. 2.6 and 2.7. The width of the curved portion of the parylene C next to the CSF was constrained to a path length of 3 mm (the actual width of the array), while the back of the array was allowed to be wider to compensate for the increased thickness.

In order to reduce the number of mesh points required in COMSOL, to avoid errors

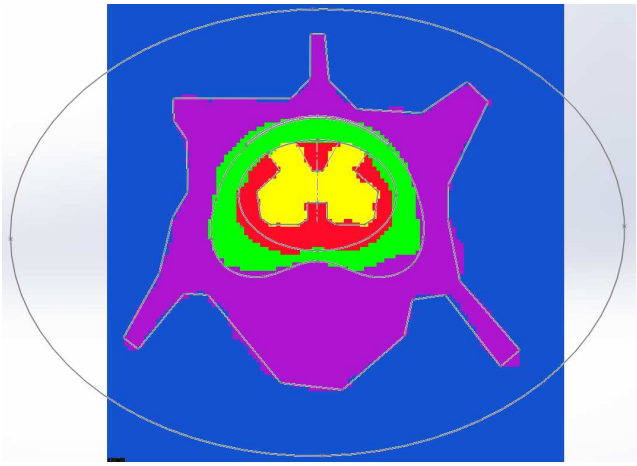

Figure 2.5: Sketch of the spinal cord geometry and electrode array on top of the segmented image. Regions in the segmented image are indicated by color: gray matter (yellow), white matter (red), CSF/roots/fibers (green), and bone (purple). See Figs. 2.6 and 2.7 for a better view of the electrode array after extrusion.

in COMSOL's meshing algorithms, and to remove the discretization of the MRI data, it was necessary to simplify the model geometry. Figure 2.5 shows a cross-section of the CAD (SolidWorks) sketch over the segmented MRI image before extrusion.

After extrusion, the electrode array model seen in Fig. 2.4 was wrapped and embossed onto the parylene C material to create holes for the electrodes. These holes were filled using constructive geometry. The result can be seen in Figs. 2.6 to 2.8.

2.1.3 Stimulation waveforms

Typically, electrical spinal stimulation uses monophasic square pulses (Parag Gad, Choe, et al., 2013), biphasic square pulses (Josef Ladenbauer, 2008), or biphasic square exponential pulses (Gill et al., 2018) where the exponential decay results from capacitive discharge. For this work, I will assume that the distance between multiple stimulation pulses is large enough that the voltage in the tissues returns to steady state for a long time relative to the pulse width so that each pulse can be analyzed separately.

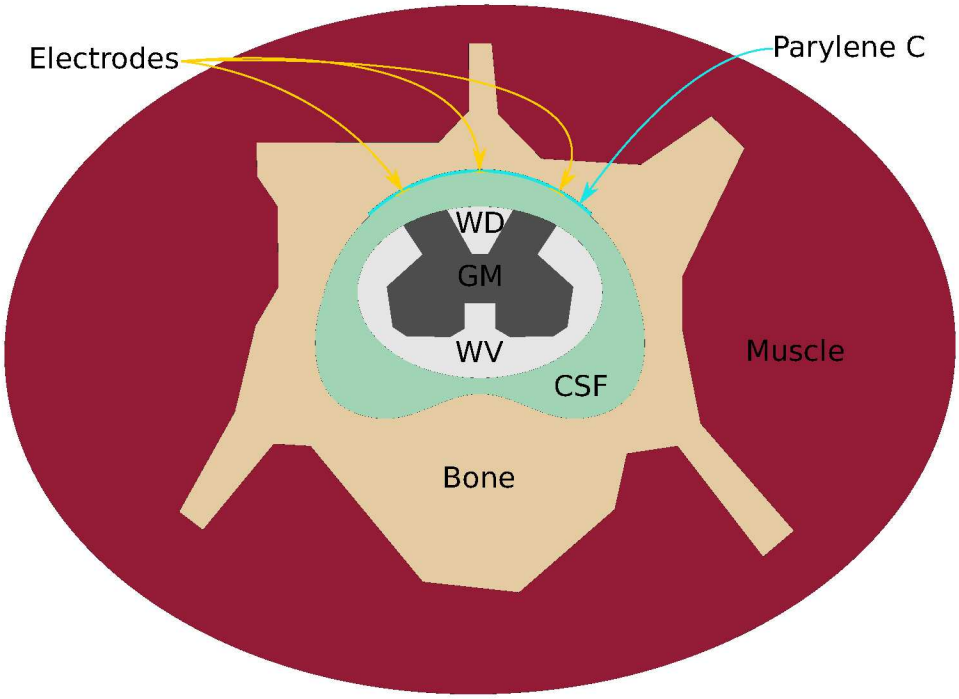

Figure 2.6: After the sketch in Fig. 2.5 was extruded to a length of 23.1 mm, 10 µm-thick electrodes were placed in the parylene. This figure shows a slice through one of the electrode rows. The cerebrospinal fluid is labeled CSF. The dorsal white matter, ventral white matter, and gray matter are labeled WD, WV, and GM respectively. See Fig. 2.7 for a close up view of the electrodes.

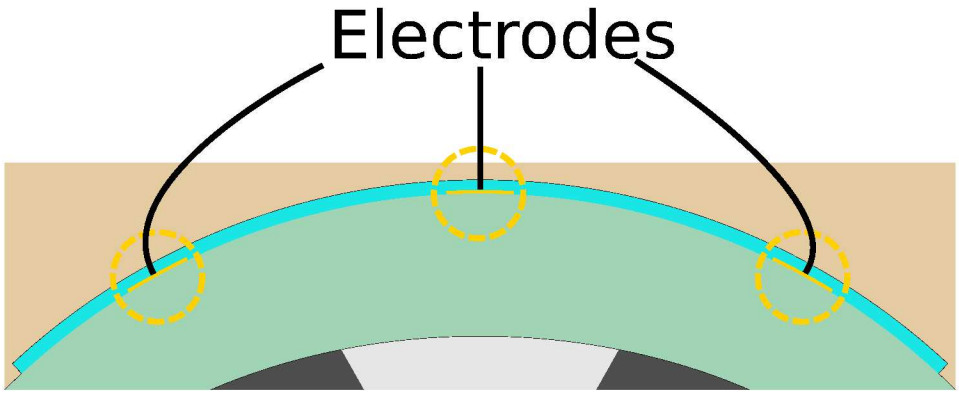

Figure 2.7: Close up view of the electrode array seen in Fig. 2.6. Electrodes are gold and indicated with dashed gold circles. The parylene C is colored cyan. See Fig. 2.6 for more details on the other materials.

Define a square monophasic pulse ($S_{\text{mono}}(t, w)$) centered at $t = 0$ with an amplitude of 1,

$$S_{\text{mono}}(t, w) = H\left(t + \frac{w}{2}\right) H\left(\frac{w}{2} - t\right), \tag{2.1}$$

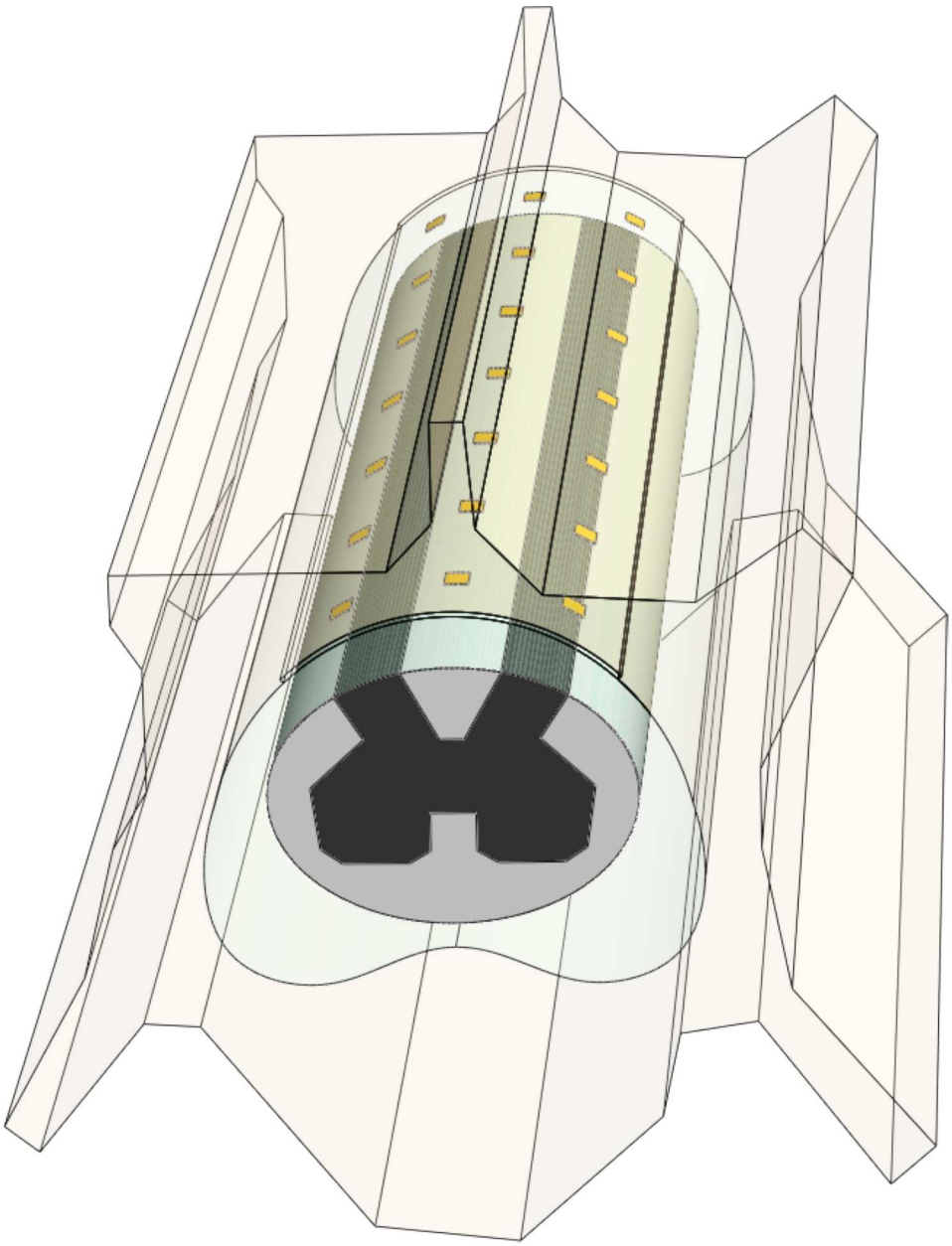

Figure 2.8: A partially transparent view of the model showing the placement of the 27 electrodes. See Figs. 2.6 and 2.7 for material labels.

where $H(.)$ is the Heaviside function, t is time in seconds, and w is the width of the pulse in seconds. Similarly, define a square biphasic pulse ($S_{\mathrm{bi}}(t, w)$) centered at $t = 0$ with an amplitude of 1,

$$S_{\mathrm{bi}}(t, w) = (2H(-t) - 1)H(t + w)H(w - t), \tag{2.2}$$

and a square exponential biphasic pulse ($S_{\text{SqExp}}(t, w)$) given by:

$$S_{\text{SqExp}}(t, w) = H(t + w)H(-t) - H(t)e^{-\frac{t}{w}}. \tag{2.3}$$

Plots of $S_{\text{mono}}(t, w)$, $S_{\text{bi}}(t, w)$, and $S_{\text{SqExp}}(t, w)$ can be seen in Figure (2.9) with $w = 200\,\mu\text{s}$.

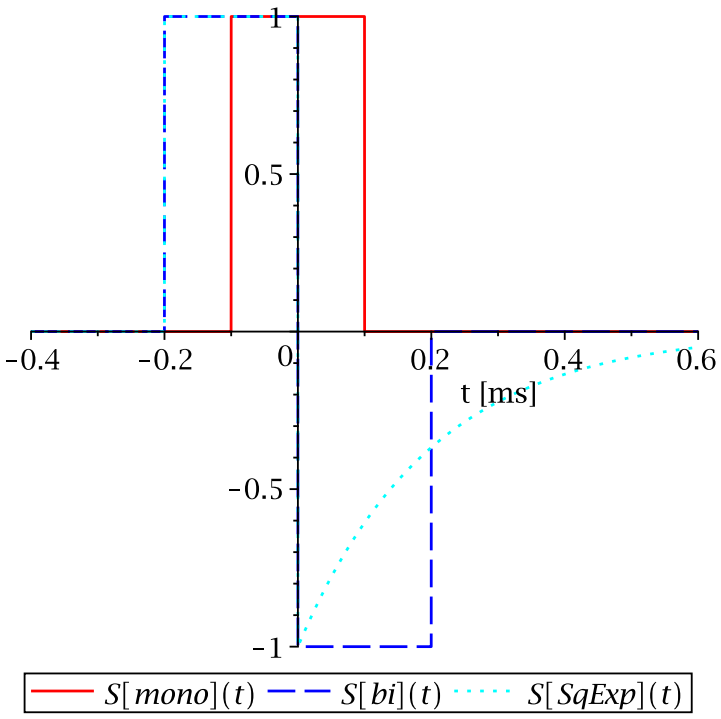

Figure 2.9: Plots of $S_{\text{mono}}(t, w = 200\,\mu\text{s})$, $S_{\text{bi}}(t, w = 200\,\mu\text{s})$, and $S_{\text{SqExp}}(t, w = 200\,\mu\text{s})$

The frequency content of the stimulation pulse is an important factor in simulating the electrical response of tissue to that stimulation pulse (as seen in Section 2.1.4). The Fourier transform ($\mathcal{F}$) can be used to convert an arbitrary time domain function $h(t)$ into a frequency domain function ($\tilde{h}(\omega)$) so that the power spectral density ($\tilde{h}^2(\omega)$) can be plotted. For this thesis, the Fourier transform ($\mathcal{F}$) is defined by:

$$\mathcal{F}(h(t)) = \int_{-\infty}^{\infty} h(t)e^{-i\omega t}dt = \tilde{h}(\omega), \tag{2.4}$$

and the inverse Fourier transform ($\mathcal{F}^{-1}$) is defined by:

$$\mathcal{F}^{-1}(\tilde{h}(\omega)) = \frac{1}{2\pi}\int_{-\infty}^{\infty}\tilde{h}(\omega)e^{i\omega t}d\omega = h(t), \tag{2.5}$$

where $\omega = 2\pi f$.

Using the above definitions, the Fourier transforms of these pulses are given by:

$$\mathcal{F}(S_{\text{mono}}(t,w)) = \tilde{S}_{\text{mono}}(f,w) = \frac{\sin(w\pi f)}{\pi f}, \tag{2.6}$$

$$\mathcal{F}(S_{\text{bi}}(t,w)) = \tilde{S}_{\text{bi}}(f,w) = 2i\frac{\sin^2(w\pi f)}{\pi f}, \tag{2.7}$$

and

$$\mathcal{F}(S_{\text{SqExp}}(t,w)) = \tilde{S}_{\text{SqExp}} = \frac{(2\pi fw - i)e^{i2\pi fw} - 4\pi fw + i}{2(i2\pi fw + 1)\pi f}. \tag{2.8}$$

Plots of $\tilde{S}^2_{\text{mono}}(f,w)$, $\tilde{S}^2_{\text{bi}}(f,w)$, and $\tilde{S}^2_{\text{SqExp}}(f,w)$ can be seen in Fig. 2.10 with $w = 200\,\mu\text{s}$.

These pulses have a broad frequency response due to the discontinuities. These discontinuities also make time-domain COMSOL simulations problematic without smoothing. In order to address both of these issues, a Gaussian was selected for a monophasic pulse (G_{mono}), and a normalized derivative of a Gaussian for a biphasic pulse (G_{bi}). In order to keep the pulses equivalent to the square monophasic and biphasic pulses, the amplitude and energy of the Gaussian pulses will be fixed to that of the equivalent square pulse. In this case, energy (E) is

$$E = \int_{-\infty}^{\infty}P(t)dt \tag{2.9}$$

where the power $P(t)$ is given by,

$$P(t) = I(t)V(t) = \frac{(V(t))^2}{R}, \tag{2.10}$$

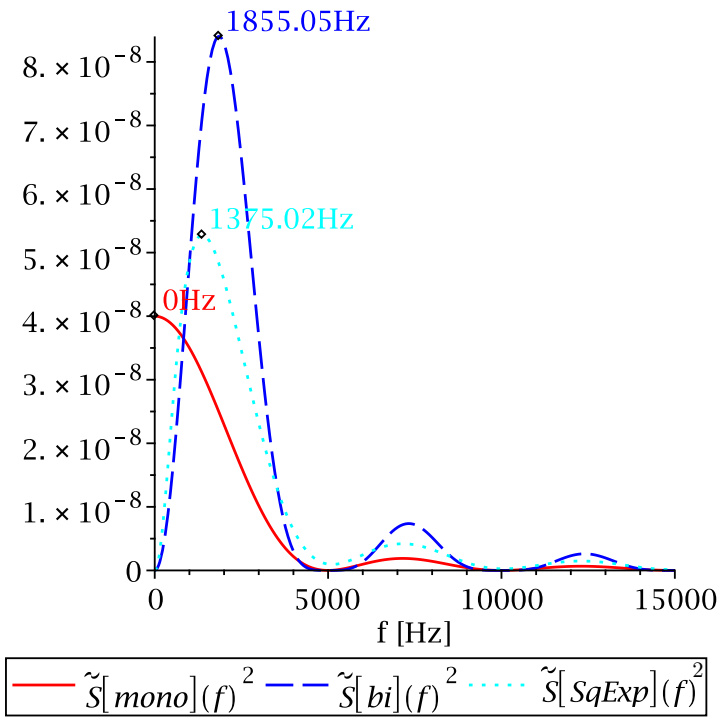

Figure 2.10: Plots of power spectral density for monophasic square pulse ($\tilde{S}^2_{\text{mono}}(f, w = 200\,\mu\text{s})$), biphasic square pulse ($\tilde{S}^2_{\text{bi}}(f, w = 200\,\mu\text{s})$), and biphasic square exponential ($\tilde{S}^2_{\text{SqExp}}(f, w = 200\,\mu\text{s})$).

$I(t) = V(t)/R$ is the current as a function of time, $V(t)$ is the voltage as a function of time, and R is a generalized resistance of the tissues. The amplitude of both square pulses is 1. The energy of the monophasic square pulse is:

$$E(S_{\text{mono}}(t, w)) = \frac{w}{R}, \tag{2.11}$$

and the energy of the biphasic square pulse is:

$$E(S_{\text{bi}}(t, w)) = \frac{2w}{R}. \tag{2.12}$$

First, define a Gaussian monophasic pulse ($G_{\text{mono}}(t, \varsigma_{\text{mono}})$) centered at $t = 0$ and

with an amplitude of $G_{\text{mono}}(0) = 1$,

$$G_{\text{mono}}(t, \varsigma_{\text{mono}}) = e^{\frac{-1}{2}\left(\frac{t}{\varsigma_{\text{mono}}}\right)^2}, \tag{2.13}$$

where ς_{mono} is a width parameter measured in seconds. The energy in this pulse is:

$$E(G_{\text{mono}}(t, \varsigma_{\text{mono}})) = \frac{\varsigma_{\text{mono}}\sqrt{\pi}}{R}. \tag{2.14}$$

So,

$$E(S_{\text{mono}}(t, w)) = E(G_{\text{mono}}(t, \varsigma_{\text{mono}})) \tag{2.15}$$

leads to:

$$\varsigma_{\text{mono}} = \frac{w}{\sqrt{\pi}}. \tag{2.16}$$

Similarly, define a Gaussian biphasic pulse ($G_{\text{bi}}(t) \propto \frac{d}{dt} G_{\text{mono}}(t)$) centered at $t = 0$ and normalized to a maximum amplitude of 1,

$$G_{\text{bi}}(t, \varsigma_{\text{bi}}) = \frac{-t}{\varsigma_{\text{bi}}} e^{\frac{1}{2}\left(1-\left(\frac{t}{\varsigma_{\text{bi}}}\right)^2\right)}. \tag{2.17}$$

The energy in this pulse is

$$E(G_{\text{bi}}(t, \varsigma_{\text{bi}})) = \frac{\varsigma_{\text{bi}}\sqrt{\pi}e}{2R}. \tag{2.18}$$

So

$$E(S_{\text{bi}}(t, w)) = E(G_{\text{mono}}(t, \varsigma_{\text{bi}})) \tag{2.19}$$

leads to:

$$\varsigma_{\text{bi}} = \frac{4w}{e\sqrt{\pi}}. \tag{2.20}$$

It can also be shown that the max and min amplitudes of the biphasic pulse occur at

$$t = \pm\varsigma_{\text{bi}}. \tag{2.21}$$

A square pulse width $w = 200\,\mu\text{s}$ corresponds in this normalization to $\varsigma_{\text{mono}} \approx 112.84\,\mu\text{s}$ and $\varsigma_{\text{bi}} \approx 166.04\,\mu\text{s}$. Plots of $G_{\text{mono}}(t, \varsigma_{\text{mono}})$ and $G_{\text{bi}}(t, \varsigma_{\text{bi}})$ can be found in Fig. 2.11.

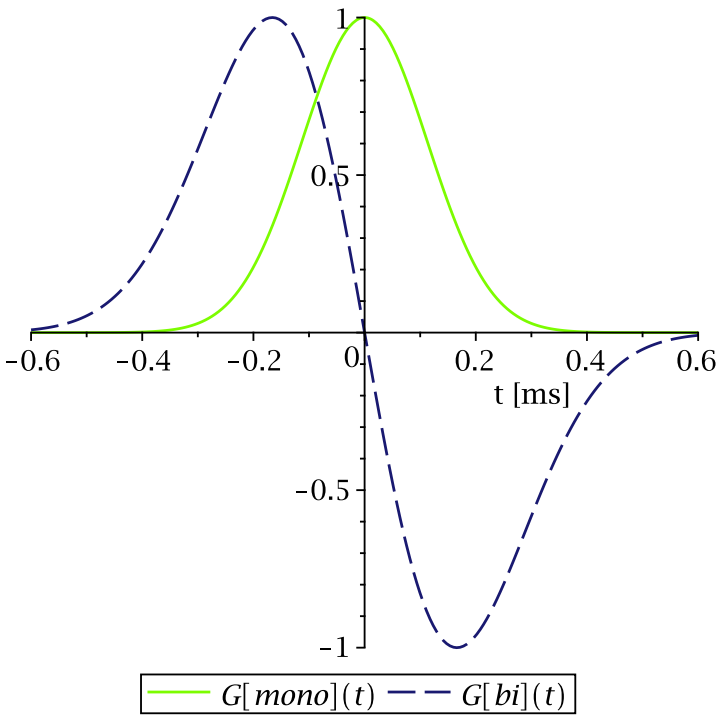

Figure 2.11: Plots of a Gaussian monophasic pulse $G_{\text{mono}}(t, \varsigma_{\text{mono}})$ and Gaussian biphasic pulse $G_{\text{bi}}(t, \varsigma_{\text{bi}})$. Where $\varsigma_{\text{mono}} \approx 112.84\,\mu\text{s}$ and $\varsigma_{\text{bi}} \approx 166.04\,\mu\text{s}$ cause $G_{\text{mono}}(t, \varsigma_{\text{mono}})$ and $G_{\text{bi}}(t, \varsigma_{\text{bi}})$ to have the same amount of power as a square pulse with width $w = 200\,\mu\text{s}$ and a biphasic square pulse with width $2w$ respectively.

The Fourier transforms of $G_{\text{bi,mono}}$ are given by:

$$\mathcal{F}(G_{\text{mono}}(t, \varsigma)) = \tilde{G}_{\text{mono}}(f, \varsigma) = \varsigma\sqrt{2\pi}e^{-2\pi^2 f^2 \varsigma^2} \tag{2.22}$$

and

$$\mathcal{F}(G_{\text{bi}}(t,\varsigma)) = \tilde{G}_{\text{bi}}(f,\varsigma) = 2\pi i\varsigma^2\sqrt{2\pi}fe^{\frac{1}{2}-2\pi^2f^2\varsigma^2}. \tag{2.23}$$

Plots of the power spectral density $\tilde{G}^2_{\text{mono}}(f,\varsigma_{\text{mono}})$ and $\tilde{G}^2_{\text{mono}}(f,\varsigma_{\text{bi}})$ can be seen in Fig. 2.12.

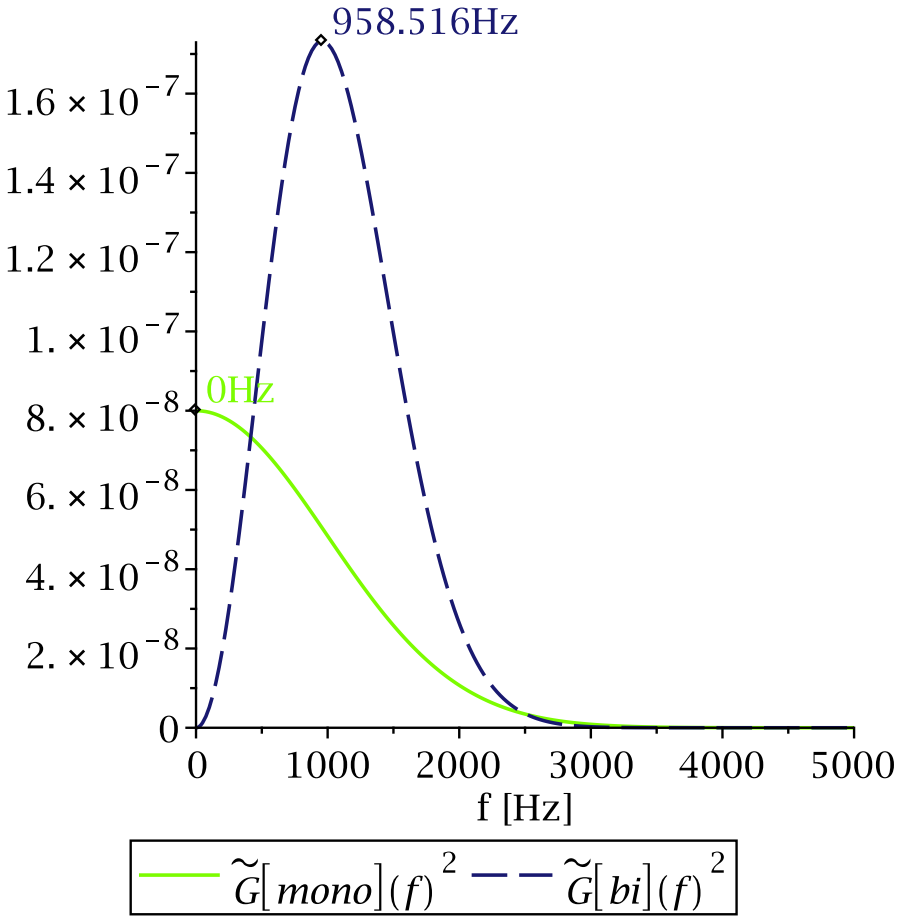

Figure 2.12: Plots of power spectral density for the monophasic Gaussian pulse $\tilde{G}_{\text{mono}}(f,\varsigma_{\text{mono}})$ and the biphasic Gaussian pulse $\tilde{G}_{\text{bi}}(f,\varsigma_{\text{bi}})$ used in this study

Unfortunately, time domain simulations in COMSOL only allow us to pick tissue electrical properties for a single frequency, so the frequencies with the most power are:

$$f^{\max}_{\text{mono}}(\varsigma) = \underset{f}{\text{argmax}}\,|\tilde{G}_{\text{mono}}(f,\varsigma)|^2 = 0 \tag{2.24}$$

and

$$f_{\text{bi}}^{\max}(\varsigma) = \underset{f}{\operatorname{argmax}} \, |\tilde{G}_{\text{bi}}(f, \varsigma)|^2 = \frac{1}{2\pi\varsigma}. \tag{2.25}$$

For the values of ς_{mono} and ς_{bi} found above, $f_{\text{mono}}^{\max} = 0$, and $f_{\text{bi}}^{\max} \approx 958.5\,\text{Hz}$.

2.1.4 Modeling tissues and electrode materials

In order to build a proper frequency-dependent simulation of epidural stimulation of the spinal cord, one must include key electrochemical properties of the affected materials, such as the relative permittivity and conductivity of the electrode array materials and biological tissues. While the relative permittivity is often referred to as the dielectric constant of the material, both conductivity and relative permittivity vary as a function of frequency and temperature. Data and 4-Cole-Cole model (K. S. Cole and R. H. Cole, 1941) fits from (C. Gabriel, 1996) will be used to model the relative permittivity and conductivity of biological tissue (Section 2.1.5.1). All materials other than muscle and white matter were modeled as isotropic materials. Data for Parylene C was taken from (Kahouli et al., 2012). The relative permittivity and conductivity of platinum were assumed to be constant in this frequency range and obtained from a CRC handbook (Chemical Rubber Company, 2012).

The rat body temperature is normally maintained between 37 °C and 38 °C (Gudjonsson, 1932), so where possible material properties have been obtained close to that temperature or adjusted for that temperature.

2.1.5 Tissues

For the model described in Section 2.1.1, it is necessary to know the frequency-dependent conductivity and relative permittivity for bone, grey matter, white matter, cerebro spinal fluid, and muscle. Additionally, the anisotropic conductivity for white matter and muscle must be taken into account.

The frequency-dependent conductivity and relative permittivity of general materials

vary with the polarizability of the material. The total polarizability of a material is the sum of the polarization of localized electrons (the electron cloud of individual atoms is distorted by the applied electric field, referred to as electronic polarizability), ionic polarizability (displacement of atoms attached with ionic bonds in response to an applied electric field), dipolar polarizability (reorientation of molecules in response to an applied electric field), and space charge polarization (long range motion of ions in response to an electric field). The polarization of a material is maximum at low frequencies when all of these types of polarization occur. See Figure 1 in (Leseal, 1982) for an overview. As the frequency of the electric field increases, the polarization decreases as the different types of polarization are unable to respond to the increased frequency. The frequency ranges at which this occurs are referred to as dispersion regions. Electronic polarizability is present at all frequencies. Ionic polarizability is limited by the speed of the displacement of the atoms and has a dispersion region around 10^{13}Hz (infrared). Dipolar polarizability is limited by the rotational speed of the dipoles and has a dispersion region around 10^{9}Hz (microwave). Space charge polarization depends on the speed of ions in the material and has a dispersion region around $10^{4} - 10^{5}$Hz (radio or lower).

In biological tissues, there are 3 commonly known dispersion regions (C. Gabriel, S. Gabriel, and Corthout, 1996): the low frequency α dispersion region associated with ionic diffusion, the β dispersion region (hundreds of kHz) associated with the polarization of cell membranes (which block the flow of ions), and the γ dispersion region (GHz) associated with the polarization of water. Other dispersion regions may exist in a particular type of tissue.

2.1.5.1 4-Cole-Cole model

The Cole-Cole model (K. S. Cole and R. H. Cole, 1941) is commonly used to fit measurements of the frequency-dependent isotropic complex relative permittivity

and conductivity of simple materials. For biological tissues it is common to use the Cole-Cole model with four dispersion regions. Three of these four dispersion regions may roughly fit the α, β, and γ regions described in Section 2.1.5, but the exact mechanisms of dispersion may differ in different types of tissues. The 4-Cole-Cole model is described by (De Geeter et al., 2012):

$$\epsilon_r(\omega) = \epsilon_\infty + \frac{\sigma_i}{i\omega\epsilon_0} + \sum_{n=1}^{4} \frac{\Delta\epsilon_n}{1 + (i\omega\tau_n)^{1-\alpha_n}}, \tag{2.26}$$

$$\sigma(\omega) = -\omega\epsilon_0 \Im(\epsilon_r(\omega)). \tag{2.27}$$

where $\epsilon_r(\omega)$ is the complex frequency-dependent relative permittivity, ϵ_∞ is the relative permittivity in the high-frequency limit, σ_i is the static conductivity arising from freely-moving charges (ions freely-moving in a liquid for example, the same ions involved in space charge polarization and the α dispersion), $i = \sqrt{-1}$, ω is the angular frequency (with units of rad/ sec), $\epsilon_0 = 8.854\,187\,817 \times 10^{-12}\,\mathrm{F\,m^{-1}}$ is the permittivity of free space[d], ($\Delta\epsilon_n$, τ_n, and α_n) are obtained by fitting experimental data, $\sigma(\omega)$ is the real valued conductivity, and $\Im(z)$ is the imaginary part of complex number z. Each term in the sum corresponds to one of the four dispersion regions.

Eqs. (2.26) and (2.27) run into non-physical numerical problems as $\omega \to 0$. These problems can be avoided by adopting the following definitions:

$$\epsilon_r(\omega) = \epsilon_\infty + \sum_{n=1}^{4} \frac{\Delta\epsilon_n}{1 + (i\omega\tau_n)^{1-\alpha_n}}, \tag{2.28}$$

$$\sigma(\omega) = \sigma_i - \omega\epsilon_0 \Im(\epsilon_r(\omega)). \tag{2.29}$$

The second term in Eq. (2.29) is the conduction from bound charges (i.e. electrons bound to molecules that are not free to move).

[d] http://physics.nist.gov/cgi-bin/cuu/Value?ep0

Gabriel et al. (C. Gabriel, 1996) found the Cole-Cole parameters for 44 biological materials (C. Gabriel and S. Gabriel, 1997) at 37 °C. Unfortunately, for some materials, in some frequency ranges, the values obtained from the 4-Cole-Cole equations can diverge significantly from nearby measured values. Fortunately, the raw data is also available for comparison (C. Gabriel and S. Gabriel, 1997). The 4-Cole-Cole parameters used in this thesis can be found in Table 2.2. Comparisons with the raw data can be found in Section 2.A. For muscle, the only available 4-Cole-Cole coefficients are for the transverse direction, even though data is available for both the parallel and transverse directions. Instead of attempting to fit the 4-Cole-Cole model to the data directly, the closest matching frequency data for "Ovine @ 37 degC" was used for the muscle.

Tissue Type	Bone (Cortical)	Grey Matter	White Matter	CSF
ϵ_∞	2.5	4	4	4
σ_i	0.02	0.02	0.02	2
$\Delta\epsilon_1$	10	45	32	65
τ_1 (ps)	13.263	7.958	7.958	7.958
α_1	0.2	0.1	0.1	0.1
$\Delta\epsilon_2$	180	400	100	40
τ_2 (ns)	79.577	15.915	7.958	1.592
α_2	0.2	0.15	0.1	0
$\Delta\epsilon_3$	5×10^3	2×10^5	4×10^4	0
τ_3 (us)	159.155	106.103	53.052	159.155
α_3	0.2	0.22	0.3	0
$\Delta\epsilon_4$	1×10^5	4.5×10^7	3.5×10^7	0
τ_4 (ms)	15.915	5.305	7.958	15.915
α_4	0	0	0.02	0

Table 2.2: Cole-Cole parameters

While there are some limited measurements of the anisotropic conductivity of CNS white matter (Ranck Jr. and BeMent, 1965), no one has measured the permittivity for white matter in both the parallel and transverse directions. For the simulations

in this thesis, I estimate the anisotropic conductivity and permittivity for the white matter using the diffusion tensor data in Table 2.3. This method assumes that ion diffusion is the dominant component of polarization at the frequencies used.

Define axes such that $+\hat{x}$ is in the right direction, $+\hat{y}$ is in the dorsal direction, and $+\hat{z}$ is in the caudal direction. This means that the eigenvectors are axis aligned such that $d_{trans} = d_{xx} = d_{yy}$, and $d_{parallel} = d_{zz}$, where $d_{\cdot}$ are the components of the diffusion tensor. Then, using the method described in (De Geeter et al., 2012), with the isotropic conductivity ($\sigma_{iso}(\omega)$) obtained from measurements or Eq. (2.29), I can obtain the conductivity in the transverse direction as follows:

$$\sigma_{trans}(\omega) = \frac{d_{trans}\sigma_{iso}(\omega)}{\sqrt[3]{d_{trans}^2 d_{parallel}}}. \tag{2.30}$$

Similarly, for the parallel direction:

$$\sigma_{parallel}(\omega) = \frac{d_{parallel}\sigma_{iso}(\omega)}{\sqrt[3]{d_{trans}^2 d_{parallel}}}. \tag{2.31}$$

Using the same method and the isotropic real relative permittivity ($\Re(\epsilon_r(\omega))_{iso}(\omega)$, where $\Re(z)$ is the real component of complex number z) again obtained from measurements or the real part of Eq. (2.28), I can obtain the real relative permittivity in the transverse direction:

$$\Re(\epsilon_r(\omega))_{trans} = \frac{d_{trans}\Re(\epsilon_r(\omega))_{iso}(\omega)}{\sqrt[3]{d_{trans}^2 d_{parallel}}}, \tag{2.32}$$

and the parallel direction

$$\Re(\epsilon_r(\omega))_{parallel} = \frac{d_{parallel}\Re(\epsilon_r(\omega))_{iso}(\omega)}{\sqrt[3]{d_{trans}^2 d_{parallel}}}. \tag{2.33}$$

Table 2.3: Diffusion tensor coefficients for rat spinal cord obtained from (Gulani et al., 1997).

Tissue Type	Measured diffusion coefficients (X $10^{-3}\frac{mm^2}{s}$)			
	d_{zz}	d_{xx}	d_{yy}	d_{xy}
Left Lateral Funiculus[a]	0.87 ± 0.04	0.23 ± 0.05	0.19 ± 0.04	−0.03 ± 0.05
Right Lateral Funiculus[a]	0.78 ± 0.03	0.18 ± 0.05	0.25 ± 0.04	−0.03 ± 0.05
Dorsal Columns[a]	1.01 ± 0.03	0.21 ± 0.03	0.25 ± 0.04	−0.06 ± 0.06
Gray Matter[a]	0.42 ± 0.02	0.44 ± 0.03	0.48 ± 0.03	−0.02 ± 0.03
Funiculus Avg[b]	0.825 ± 0.03	0.205 ± 0.04	0.22 ± 0.03	−0.03 ± 0.04

[a] (Gulani et al., 1997)
[b] Average of left and right lateral funiculus

2.1.6 Electrode array

Since the electrode array is made with parylene C and platinum traces, the conductivity ($\sigma(\omega)$) and relative permittivity ($\Re(\epsilon_r(\omega))$) of these materials are important to the modeling effort.

2.1.6.1 Parylene C

Data on the real part of the dielectric constant and the dissipation factor (D_F) were obtained from the as-deposited values at 25 °C in Figure 5 of Kahouli (2012) (Kahouli et al., 2012) and fit to a polynomial in $\Lambda = \log_{10}(fs)$.

$$\begin{aligned} D_F(\Lambda) =& 0.061018 - 2.912\times10^{-5}\Lambda - 0.0015511\Lambda^2 + 0.00089049\Lambda^3 - 0.00059251\Lambda^4 + 2.0756\times10^{-5}\Lambda^5 + 5.9074\times10^{-5}\Lambda^6 \\ & - 1.2942\times10^{-5}\Lambda^7 - 6.965\times10^{-8}\Lambda^8 + 2.5675\times10^{-7}\Lambda^9 - 1.9506\times10^{-8}\Lambda^{10} \end{aligned} \tag{2.34}$$

$$\begin{aligned} \Re(\epsilon_r(\Lambda)) =& 4.1276 - 0.28559\Lambda - 0.0078781\Lambda^2 - 0.0046379\Lambda^3 + 0.0054592\Lambda^4 + 0.0013196\Lambda^5 - 0.0024512\Lambda^6 \\ & + 0.0010473\Lambda^7 - 0.00021781\Lambda^8 + 2.2709\times10^{-5}\Lambda^9 - 9.492\times10^{-7}\Lambda^{10} \end{aligned} \tag{2.35}$$

The dissipation factor (D_F)[e] quantifies the dielectric's dissipation of electromag-

[e]The dissipation factor, D_F, is also called the loss tangent in some literature, usually with the notation $\tan\delta$.

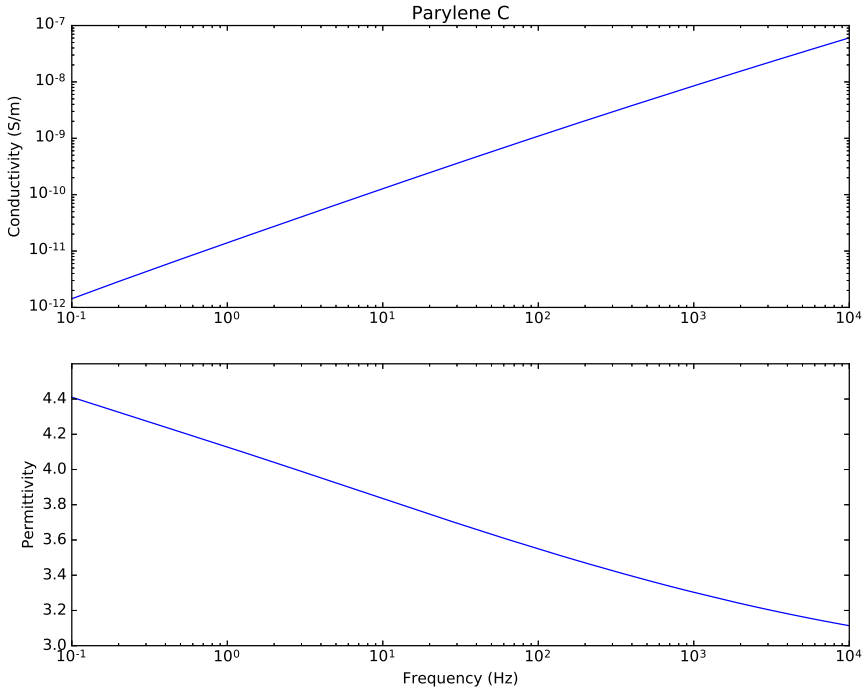

Figure 2.13: Conductivity and real relative permittivity for parylene C

netic energy as heat and is given by (Orfanidis, 2016):

$$D_F = \frac{\sigma_i - \omega\epsilon_0 \Im(\epsilon_r)}{\omega\epsilon_0 \Re(\epsilon_r)}. \tag{2.36}$$

The numerator in Eq. (2.36) can be recognized from Eq. (2.29), and so the following equation can be derived for conductivity:

$$\sigma(\omega) = D_F \omega\epsilon_0 \Re(\epsilon_r). \tag{2.37}$$

Based on Eqs. (2.34), (2.35) and (2.37), the conductivity and real relative permittivity of Parylene C are plotted in Fig. 2.13.

2.1.6.2 Platinum

The CRC Handbook of Chemistry and Physics (Chemical Rubber Company, 2012) lists the resistivity of platinum at 27 °C as $10.8 \times 10^{-8}\,\Omega\,\mathrm{m}$. This gives a conductivity of $\sigma = 9.26 \times 10^{6}\,\mathrm{S\,m^{-1}}$. The real part of the relative permittivity was set to 1 as is customary for metals. These values are assumed to be fairly frequency-independent below optical frequencies (Scheffler et al., 2005).

2.1.7 Materials Summary

Table 2.4: Conductivity values with units $\mathrm{S\,m^{-1}}$

Material	$\sigma^{0\,\mathrm{Hz}}_{parallel}$	$\sigma^{0\,\mathrm{Hz}}_{transverse}$
Bone	0.02	
CSF	2	
Gray matter	0.02	
Muscle	0.24[a]	0.22[a]
Parylene C	1.42×10^{-12}[b]	
Platinum	9259259.25926	
WM (Dorsal Columns)	0.054	0.012
WM (Lateral & Ventral Funiculus)	0.049	0.013
Material	$\sigma^{958.5\,\mathrm{Hz}}_{parallel}$	$\sigma^{958.5\,\mathrm{Hz}}_{transverse}$
Bone	0.02	
CSF	2	
Gray matter	0.099	
Muscle	0.52[c]	0.34[c]
Parylene C	8.20×10^{-9}[d]	
Platinum	9259259.25926	
WM (Dorsal Columns)	0.17	0.038
WM (Lateral & Ventral Funiculus)	0.15	0.040

[a] f=10.0 Hz (closest frequency for ovine @37 degC muscle data)
[b] f=0.1 Hz (closest frequency for parylene C data)
[c] f=1000.0 Hz (closest frequency for ovine @37 degC muscle data)
[d] f=959.0 Hz (closest frequency for parylene C data)

2.2 COMSOL simulations

A Matlab program was written using the COMSOL Matlab interface to import the SolidWorks model, label the various materials in the model, and set the ma-

Table 2.5: Real relative permittivity values (unit less)

Material	$er^{0\,\mathrm{Hz}}_{parallel}$	$er^{0\,\mathrm{Hz}}_{transverse}$
Bone	110000	
CSF	110	
Gray matter	45000000	
Muscle	83000000[a]	41000000[a]
Parylene C	4.410[b]	
Platinum	1	
WM (Dorsal Columns)	94000000	21000000
WM (Lateral & Ventral Funiculus)	87000000	22000000
Material	$er^{958.5\,\mathrm{Hz}}_{parallel}$	$er^{958.5\,\mathrm{Hz}}_{transverse}$
Bone	2800	
CSF	110	
Gray matter	170000	
Muscle	1200000[c]	590000[c]
Parylene C	3.307[d]	
Platinum	1	
WM (Dorsal Columns)	190000	44000
WM (Lateral & Ventral Funiculus)	180000	46000

[a] f=10.0 Hz (closest frequency for ovine @37 degC muscle data)
[b] f=0.1 Hz (closest frequency for parylene C data)
[c] f=1000.0 Hz (closest frequency for ovine @37 degC muscle data)
[d] f=959.0 Hz (closest frequency for parylene C data)

terial properties as summarized in Tables 2.4 and 2.5. The mesh was set to "Extra fine" and can be seen in Fig. 2.14. The outside boundaries (extruded oval shaped) were set to be insulating (Neumann boundary condition), i.e. no current passing through them. For active electrodes, the voltage of the back surface of the electrode was set to the stimulating waveform (Dirichlet boundary condition). No voltage or current restrictions were placed on the non-active electrodes. Static (time invariant inputs) simulations were used for comparison and testing purposes. For time domain simulations, the time step (Δt) was set to 0.01 ms and solved for time $t_{bi,mono} = -10\varsigma_{bi,mono} \cdots + 10\varsigma_{bi,mono}$. For biphasic stimulation, $\varsigma_{bi} = 0.166\,04$ ms so the COMSOL simulation was run from simulation time $t_{bi} = -1.6604$ ms to $t_{bi} = 1.6604$ ms. For monophasic stimulation, $\varsigma_{mono} = 0.112\,84$ ms so the COM-

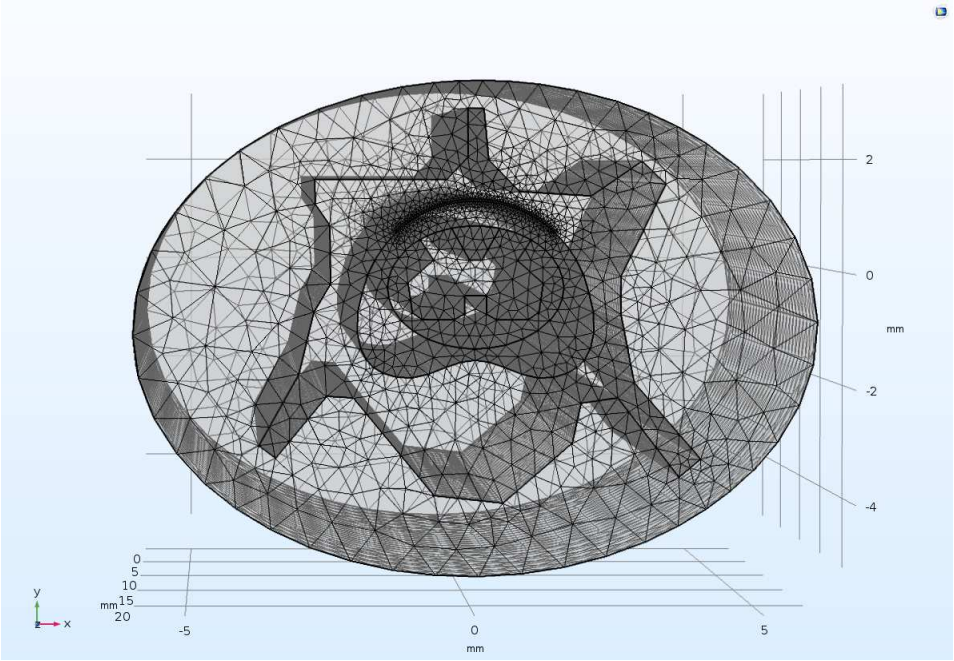

Figure 2.14: The finite element mesh used in all the volume conductor simulations.

SOL simulation was run from simulation time $t_{mono} = -1.1284$ ms to 1.1284 ms. After the simulations were complete, voltage time series were extracted from points corresponding to each segment of the neurons as will be described in Chapter 3.

2.2.1 Stimulation patterns

Although more complex patterns of the active stimulating electrodes are possible and have been used in humans (Harkema et al., 2011), for this thesis I will only consider bipolar combinations of electrodes. Each combination will be referred to by a name consisting of [positive electrode name][p for positive sign][negative electrode name][n for negative sign]. Each name implies a pair of equations. For example, combination A2pC5n means that the stimulation voltage on the back surface of the A2 and C5 electrodes are defined, respectively, by:

$$V_s^{\mathrm{A2}} = V_S G(t) \tag{2.38}$$

$$V_s^{\mathrm{C5}} = -V_S G(t), \tag{2.39}$$

where V_s is the stimulation scale factor (can be positive or negative with units of volts), and $G(t)$ is the stimulation shape function (either $G_{bi}(t)$ for biphasic stimulation or $G_{mono}(t)$ for monophasic stimulation (see Section 2.1.3 for definitions)). Electrodes not referenced in the combination name are simulated as floating. See Table 2.1 for electrode labels and array orientation. Figures 4.1 and 4.2 show the labeled electrode array in the simulated spinal cord.

The COMSOL simulations are linear so all simulations can be done with $V_s = 1\,\mathrm{V}$ and the output scaled for other voltages. For the electrode array described in Section 2.1.1 (3 columns and 7 rows), there are 210 unique bipolar combinations (considering that the combination A1pB1n ($V_s^{\mathrm{A1}} = V_S G(t)$, $V_s^{\mathrm{B1}} = -V_S G(t)$) is a scalar multiple of B1pA1n ($V_s^{\mathrm{B1}} = V_S G(t)$, $V_s^{\mathrm{A1}} = -V_S G(t)$). Since the model is an extrusion, the combinatorial number of simulations necessary can be reduced if translations of combinations of electrodes along the $\hat{z}$ direction result in the same output. To test this, I will compute stationary simulations for all three possible single row combinations (ANpBNn, ANpCNn, BNpCNn) for each row N and compare extracted voltage points under that row with the center row. Extracted points correspond to each segment in the neurons described in Chapter 3 (including all 6 axons directions). Figure 4.2 shows the locations of these neurons with the axons in the $-\hat{x}$ direction. The histogram results in Fig. 2.15 show that there are edge effects in rows 1 and 7. However, translations along the $\hat{z}$ axis between rows 2-6 result in nearly the same output. In this thesis, I will only consider combinations ignoring rows 1 and 7 to avoid edge effects.

Although the spinal cord model is not completely symmetric across the $x = 0$ plane (the bone and muscle geometry captured from the MRI data are not symmetric), it would be useful to test the difference between mirrored combinations. If the difference is small, then symmetry about the mid-line can be used to reduce the required number of simulations. The histogram of the difference between combina-

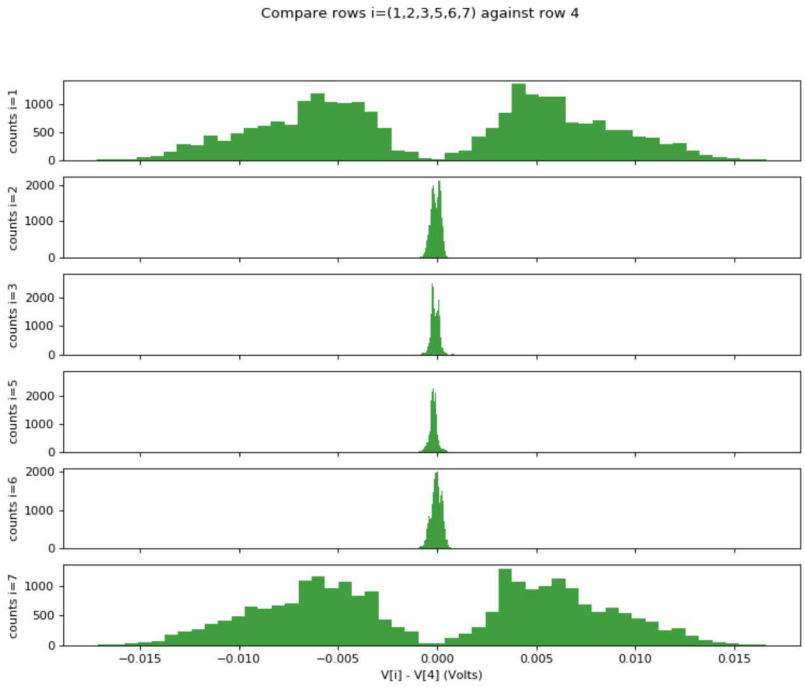

Figure 2.15: Comparison of combination translations along the $\hat{z}$ axis. Note the edge effects in row 1 and 7. The histogram includes all three single row combinations (ANpBNn,ANpCNn,BNpCNn) (where N is the row number) and stationary simulations run at $f_{\text{mono}}^{\text{max}} = 0\,\text{Hz}$ and $f_{\text{bi}}^{\text{max}} \approx 958.5\,\text{Hz}$.

tion A4pB4n and the mirrored output from B4nC4p can be seen in Fig. 2.16. These results show that there is a mean difference of 0.229 mV between these simulations. The maximum difference between these simulations was 1.49 mV. If these simulations are scaled by a factor of ±10 to reach maximum stimulation voltages of ±10 V, these differences would also be scaled by the same factor. This gives some idea of how much the results might change with differing physical geometry. While future studies may explore these geometry effects, the low differences support the use of symmetry.

Table 2.6 shows the number of unique bipolar combinations given different numbers of rows and different sets of assumptions. Given the previous discussion, edge rows are not used due to edge effects (5 active rows). Allowing $\hat{z}$ translations and mirroring across both the x=0 and z=0 planes yields 18 unique bipolar simulations:

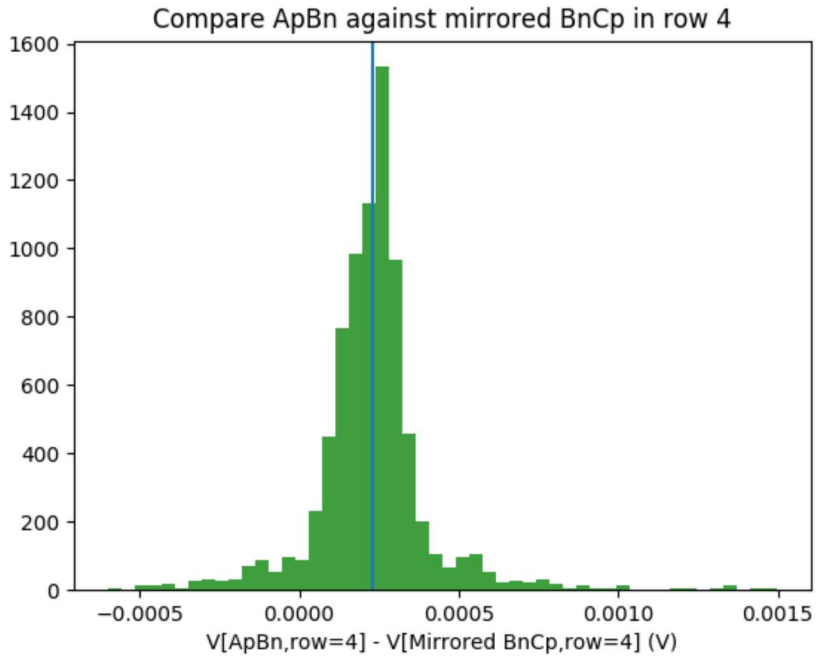

Figure 2.16: Comparison of combination ($A4 = 1V, B4 = -1V$) with mirrored combination ($C4 = 1V, B4 = -1V$). The mean difference is 0.229 mV (indicated by vertical line) and the maximum difference was 1.49 mV. The histogram includes stationary simulations run at $f_{\text{mono}}^{\text{max}} = 0\,\text{Hz}$ and $f_{\text{bi}}^{\text{max}} \approx 958.5\,\text{Hz}$.

A2pA6n, A2pB6n, A2pC6n, A3pA5n, A3pA6n, A3pB5n, A3pB6n, A3pC5n, A3pC6n, A4pA5n, A4pB4n, A4pB5n, A4pC4n, A4pC5n, B2pB6n, B3pB5n, B3pB6n, and B4pB5n.

Table 2.6: Number of unique bipolar combinations

# of rows	all bipolar	A	B	C	D
1	3	3	3	2	2
2	15	12	9	7	6
3	36	21	15	12	10
4	66	30	21	17	14
5	105	39	27	22	18
6	153	48	33	27	22
7	210	57	39	32	26

[A] allowing $\hat{z}$ translations
[B] allowing $\hat{z}$ translations and mirroring across the z=0 plane
[C] allowing $\hat{z}$ translations and mirroring across the x=0 plane
[D] allowing $\hat{z}$ translations and mirroring across both the x=0 and z=0 planes

2.2.2 Computational details

Simulations were conducted using COMSOL 5.1 and MATLAB R2012a on a machine with 94G RAM and dual Intel® Xeon® X5550 CPUs operating at 2.67GHz. Each biphasic simulation (i.e. one combination) on average took 5.5 ± 0.2 hours. Each monophasic simulation on average took 2.8 ± 0.1 hours. For the biphasic stimulation, the time series extraction on average took 4.73 ± 0.07 minutes for each combination. For monophasic, the same extraction took on average 3.22 ± 0.3 minutes.

2.3 Summary

In this chapter, I discussed the finite element model of the rat lumbosacral spinal cord and electrode array that will be used in the rest of the thesis. The geometry of the finite element model was derived from an extrusion of a transverse slice of an MRI image of the L1 vertebra. Stimulation waveforms were analyzed for their dominant frequency components, and material properties (conductivity and permittivity) were selected using the main frequency component of each stimulation waveform. The finite element model was validated by comparing extracted voltage values for translated single row combinations and mirrored combinations which should result in the same voltage potentials.

2.A Appendix: Conductivity and relative permittivity measurements from literature compared with 4-cole-cole fits

Conductivity and relative permittivity measurements for bone, CSF, gray matter, muscle, and isotropic white matter from a variety of animals and original authors were obtained from (C. Gabriel and S. Gabriel, 1997). 4-Cole-Cole parameters for these materials were also obtained from the same source. Conductivity values from (Josef Ladenbauer, 2008) were also obtained for comparison.

The collected data for muscle is presented in Fig. 2.17. Parameters for a 4-Cole-

Cole fit are only available for transverse muscle even though data is available for parallel muscle. At frequencies below 1 kHz, there is about an order of magnitude variation in the conductivity and 2 orders of magnitude in the permittivity variation. There also appears to be significant differences in the amount of anisotropy found in the different studies.

The collected data for bone is presented in Fig. 2.18. It shows variation of 2 orders of magnitude in both conductivity and relative permittivity below 1 kHz, depending on the type of bone and the animal source.

Figure 2.19 plots the very limited data available for cerebro spinal fluid (CSF). The value that Ladenbauer used for the CSF ($1.7\,\mathrm{S\,m^{-1}}$ @ 1000 Hz) is certainly closer in frequency to the dominant frequencies of the stimulation waveforms used in this thesis than the data used for the 4-Cole-Cole fit, but the corresponding relative permittivity was not available, so the value ($2\,\mathrm{S\,m^{-1}}$) obtained from the 4-Cole-Cole fit was used instead.

Figure 2.20 presents the conductivity and permittivity of white matter. At high frequencies the conductivity and permittivity of white matter appears to be conserved across species and studies. The values of conductivity used in (Josef Ladenbauer, 2008) (from a cat) appear to be significantly larger than those found by Gabriel et al. in a sheep.

Figure 2.21 shows the collected data for gray matter. The grey matter values appear to have minimal variation across species and samples at high frequencies. The conductivity of grey matter used in (Josef Ladenbauer, 2008) also seems high compared with the values Gabriel et al. found in a sheep.

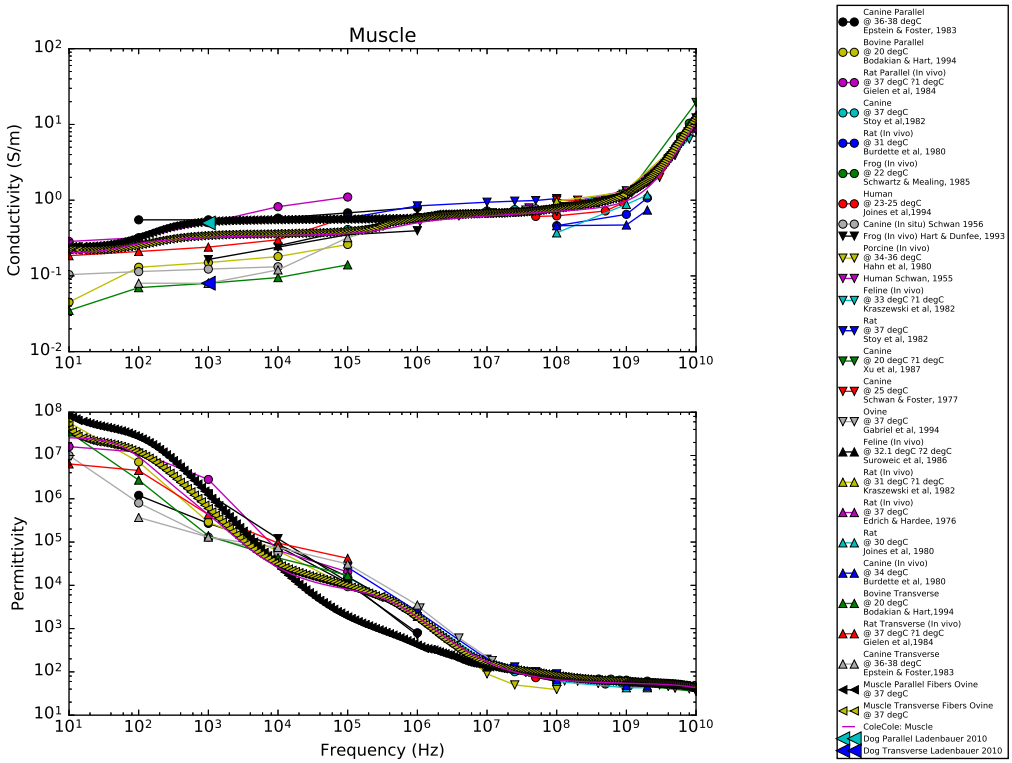

Figure 2.17: Data and Cole-Cole fits for Muscle. The 4-Cole-Cole fit is only for transverse muscle even though data is available for both parallel and transverse. Data from (C. Gabriel and S. Gabriel, 1997) and (Josef Ladenbauer, 2008).

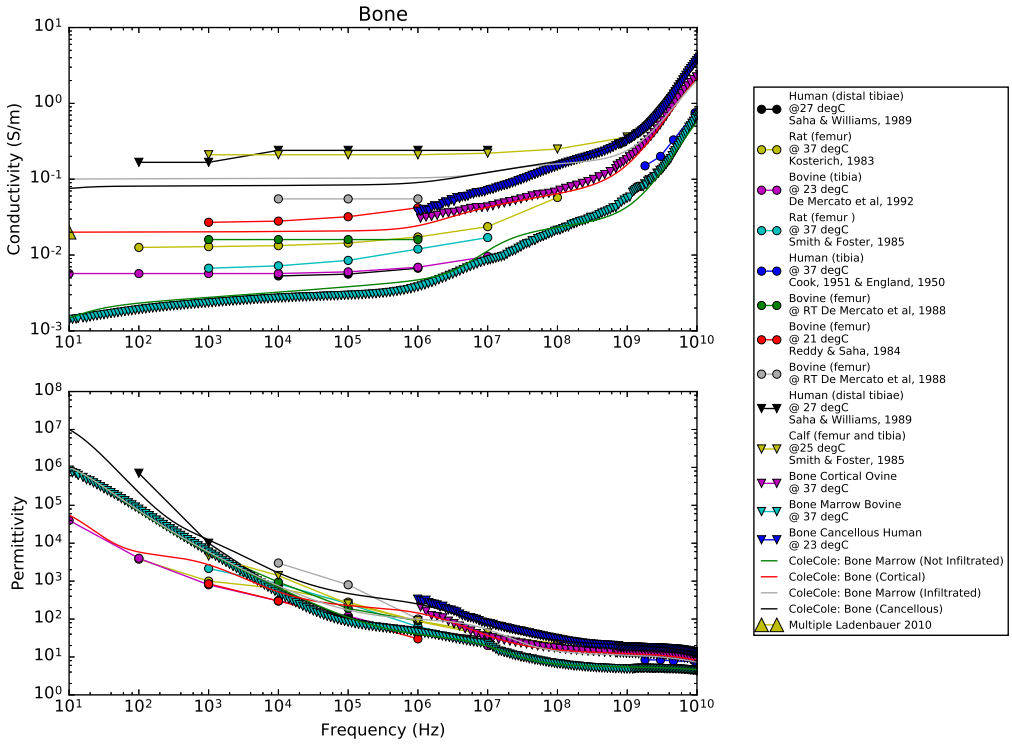

Figure 2.18: Data and Cole-Cole fits for bone. Data from (C. Gabriel and S. Gabriel, 1997) and (Josef Ladenbauer, 2008).

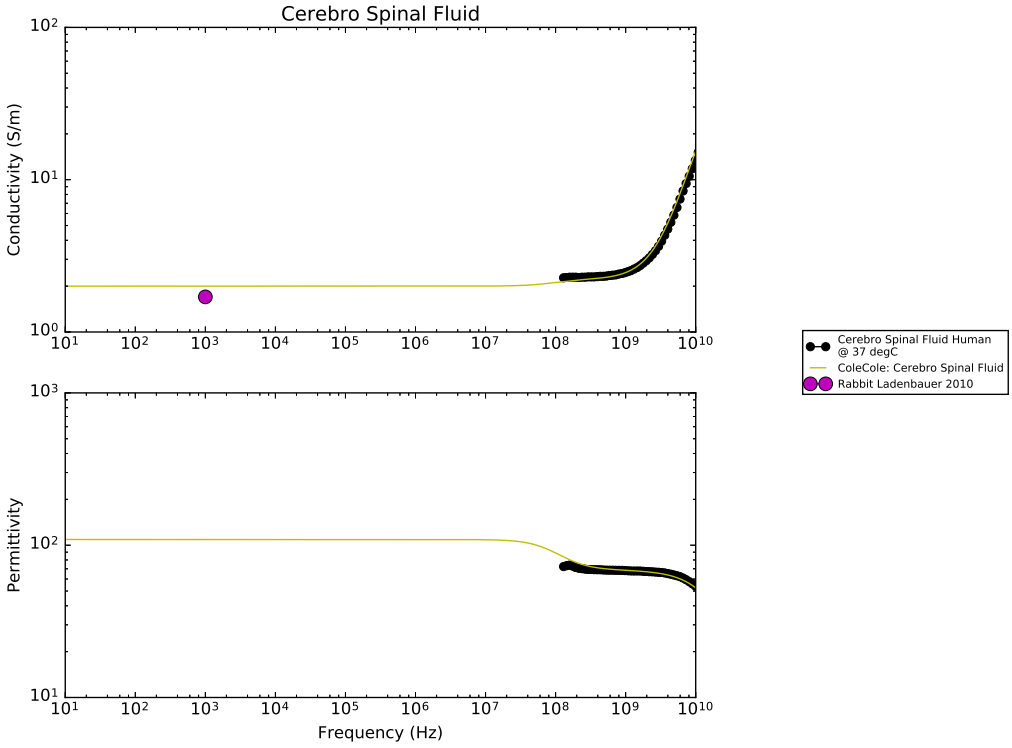

Figure 2.19: Data and Cole-Cole fits for cerebro spinal fluid (CSF). Data from (C. Gabriel and S. Gabriel, 1997) and (Josef Ladenbauer, 2008).

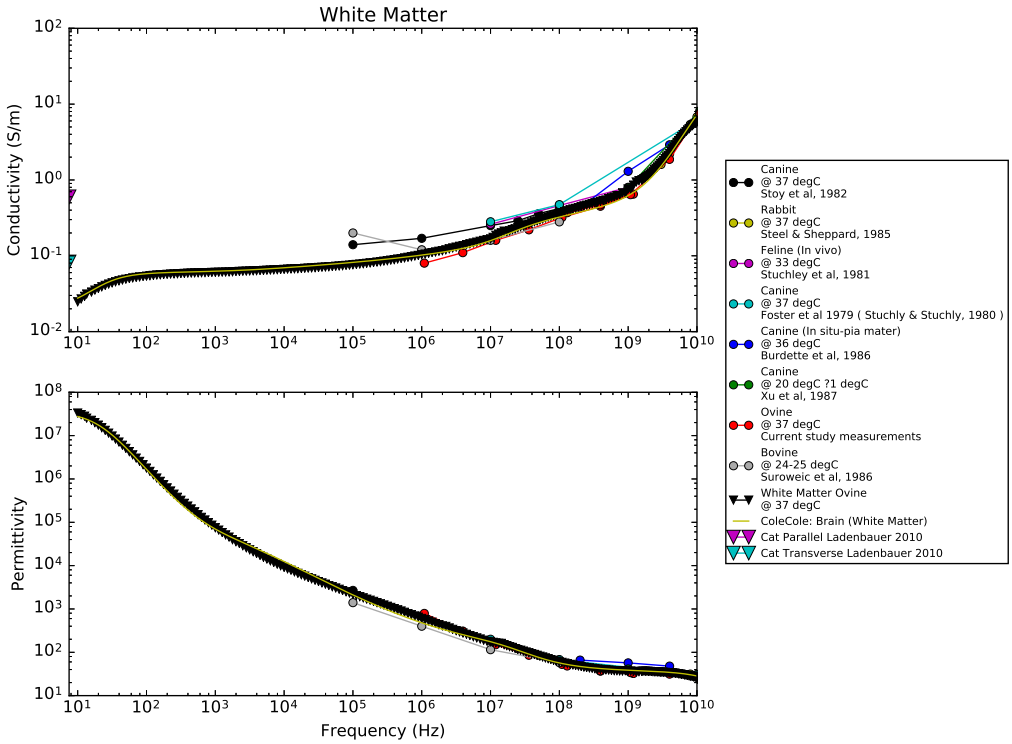

Figure 2.20: Data and Cole-Cole fits for isotropic white matter. Data from (C. Gabriel and S. Gabriel, 1997) and (Josef Ladenbauer, 2008).

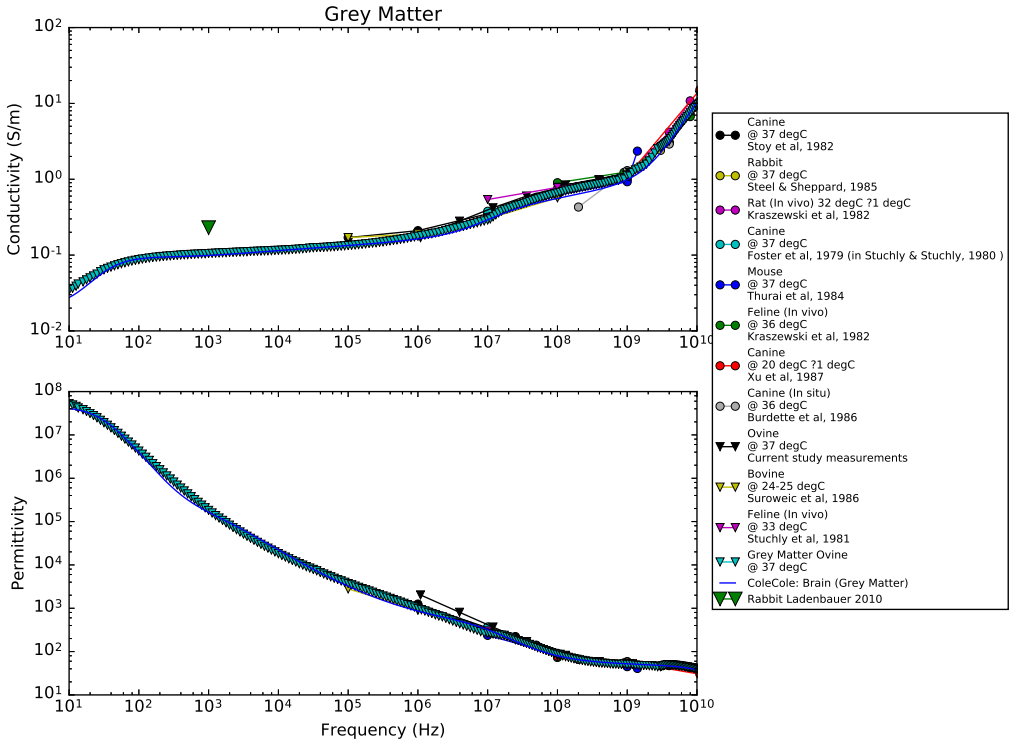

Figure 2.21: Data and Cole-Cole fits for gray matter. Data from (C. Gabriel and S. Gabriel, 1997) and (Josef Ladenbauer, 2008).